Synthesis and Properties of Electrically Conductive, Ductile, Extremely Long (~50 μm) Nanosheets of $K_xCoO_2 \cdot yH_2O$

Mahmut Aksit, Benjamin C. Hoselton, Ha Jun Kim, Don-Hyung Ha, and Richard D. Robinson*

Cornell University, Department of Materials Science and Engineering, 214 Bard Hall, Ithaca, New York 14853, United States

Ⓢ *Supporting Information*

ABSTRACT: Extremely long, electrically conductive, ductile, free-standing nanosheets of water-stabilized $K_xCoO_2 \cdot yH_2O$ are synthesized using the sol−gel and electric-field induced kinetic-demixing (SGKD) process. Room temperature in-plane resistivity of the $K_xCoO_2 \cdot yH_2O$ nanosheets is less than ~4.7 mΩ·cm, which corresponds to one of the lowest resistivity values reported for metal oxide nanosheets. The synthesis produces tens of thousands of very high aspect ratio (50,000:50,000:1 = length/width/thickness), millimeter length nanosheets stacked into a macro-scale pellet. Free-standing nanosheets up to ~50 μm long are readily delaminated from the stacked nanosheets. High-resolution transmission electron microscopy (HR-TEM) studies of the free-standing nanosheets indicate that the delaminated pieces consist of individual nanosheet crystals that are turbostratically stacked. X-ray diffraction (XRD) studies confirm that the nanosheets are stacked in perfect registry along their *c*-axis. Scanning electron microscopy (SEM) based statistical analysis show that the average thickness of the nanosheets is ~13 nm. The nanosheets show ductility with a bending radius as small as ~5 nm.

KEYWORDS: nanosheets, electrical conductor, metal oxide, turbostratic, HR-TEM, ductile, high anisotropy
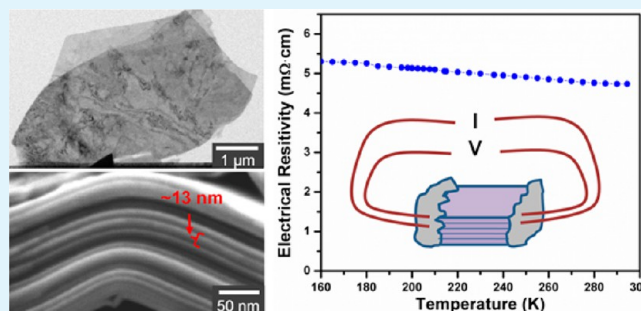
■ INTRODUCTION

Ultrathin metal oxide sheets can exhibit quantum size and surface effects that result in novel electronic, ferromagnetic, magneto-optical, electrochemical, catalytic, and photoresponsive properties.[1−10] However, large scale synthesis of inorganic, free-standing two-dimensional (2D) nanosheet materials still remains a challenge, especially with compounds, such as transition metal oxides.[3−5,11]

Free-standing nanosheets of transition metal oxides have exciting technological implications and are promising candidates for replacing conventional thin films in certain applications. 2D metal oxide nanosheets can provide extremely large surface areas with high chemical and mechanical durability, leading to efficient charge storage. For instance, (1) lithium-ion battery cathodes of nanoporous $LiMn_2O_4$ nanosheets display superior cycling performance compared to bulk $LiMn_2O_4$ at high charge−discharge rates,[12] (2) octatitanate nanosheets have better reversible capacities than those of conventional octatitanate, presumably because of the ability of the nanosheets to better withstand damage caused by lithium insertion,[13,14] and (3) highly efficient and stable pseudocapacitive cathodes have been obtained from $K_{0.15}MnO_2 \cdot 0.43H_2O$ nanosheets.[15] Especially for nanoscale high-κ dielectrics, free-standing metal oxide nanosheets perform better than metal oxide thin films grown by conventional vapor deposition techniques, which tend to show decreasing dielectric constants with decreasing film thickness.[16,17] For example, <10 nm thick nanosheets of $Ti_{0.87}O_2$, $Ca_2Nb_3O_{10}$, and $Sr_2Nb_3O_{10}$ used as gate dielectric layers provided high dielectric constants ($\varepsilon_r \approx 125$, 210, and 240, respectively) and very low leakage current densities in FET (field emission transistor) devices.[3,18] Metal oxide nanosheets can also be utilized as semiconducting materials in microelectronic devices as previously demonstrated with FET semiconducting channels made from $Ti_{0.91}O_2$ nanosheets.[3] Free-standing metal oxide nanosheets have the advantage of being solution processable, allowing deposition on substrates for device integration. Because they do not need to be grown on a substrate, free-standing nanosheets have different boundary and surface conditions from conventional thin films, which can result in useful physical properties.

Producing free-standing 2D nanostructures of alkali cobaltates is difficult to achieve by the conventional method for nanosheet synthesis, chemical exfoliation, because the chemical treatment usually causes complete depletion of alkali content from the crystal structure, resulting in CoO nanosheets.[3,5,19] In our recent study, we reported millimeter-length, high aspect ratio nanosheets of Na_xCoO_2, which could be readily delaminated into free-standing nanosheets without changing crystal structure.[20] As an atomically layered complex metal oxide, bulk Na_xCoO_2 has fascinating stoichiometric-dependent properties such as a high thermoelectric power factor and high electrical conductivity.[21−26] Nanosheets of

Na_xCoO_2 could result in improved thermoelectric performance compared to bulk because of phonon scattering and confinement effects,[27] and they could be used as conductive supports for electrocatalytic applications due to their high surface area and high oxidation resistance.[28] Nanosheets of K_xCoO_2 should also be important for practical applications because of the similarities between K_xCoO_2 and Na_xCoO_2 in terms of the crystal family (hexagonal), host atomic layer (CoO_2 octahedra), and intercalating atomic species (alkali metals).[29,30]

K_xCoO_2 has a similar crystal structure[30] to Na_xCoO_2 and has also been researched for its desirable electronic transport properties. The number of studies of K_xCoO_2, however, is limited, likely due to the extreme hygroscopicity of K_xCoO_2.[30−33] K_xCoO_2 consists of two-dimensional triangular CoO_2 layers with K^+ ion intercalated between the layers.[30] The K/Co ratio and the sites occupied by K^+ ions in the crystal vary with the different phases (x) of K_xCoO_2.[33] At room temperature, the charge-ordered hexagonal $K_{4/7}CoO_2$ phase has the lowest electrical resistivity ($\sim$10 m$\Omega\cdot$cm) among the phases of K_xCoO_2,[33] whereas the largest Seebeck coefficient (thermopower) was observed for the rhombohedral $K_{0.5}CoO_2$ phase ($\sim$30 μV/K).[30] Tang et al. reported that the water stabilized $K_{0.35}CoO_2\cdot0.34H_2O$ phase has $\sim$4 times lower electrical resistivity ($\sim$2.3 m$\Omega\cdot$cm) compared to the $K_{4/7}CoO_2$ phase.[34] Besides having lower electrical resistivity, $K_{0.35}CoO_2\cdot0.34H_2O$ is also more stable under atmospheric conditions compared to the anhydrous K_xCoO_2 phases. The high electrical conductivity and atmospheric stability of $K_{0.35}CoO_2\cdot0.34H_2O$ make it a promising candidate for practical applications.

Extremely long ($>$50 μm), bendable nanosheets of electrically conductive $K_xCoO_2\cdot yH_2O$ are of particular interest because they can be utilized in metal oxide nanoelectronics as electrical conductors.[3] Although many metal oxide nanosheets have been reported in the literature for use in oxide nanoelectronics, the majority of these nanosheets are either semiconductors or insulators with dielectric properties.[3,35] The number of studies on high electrical conductivity metal oxide nanosheets has been limited.[36,37] Among the metal oxide nanosheets in the literature, RuO_2 nanosheets are the only room temperature electrical conductors with a low sheet resistance (R_s), at 12 kΩ sq^{-1} for a 1.38 nm thick (t) single layer (corresponding to a resistivity value of $\rho = R_s t \approx 1.7$ m$\Omega\cdot$cm) and 0.36 kΩ sq^{-1} for a ten-layered film ($\rho = R_s t \approx 0.5$ m$\Omega\cdot$cm, assuming $t \approx 13.8$ nm).[36] However, the lateral sizes of these nanosheets are smaller than several micrometers, and making them impractical for large-scale electronic devices. Here we report $K_xCoO_2\cdot yH_2O$ nanosheets that could readily serve as long and flexible electrical conductors for metal oxide nanoelectronics because of their large lateral lengths (micrometer to millimeter scales), relatively high electrical conductivity, and extreme ductility.

In this work, scalable nanomanufacturing of electrically conductive $K_xCoO_2\cdot yH_2O$ nanosheets is reported for the first time. The synthesis method is based on the new sol−gel chemistry and electric-field induced kinetic-demixing (SGKD) process.[20] The final product consists of tens of thousands of well-defined nanosheets that are stacked into a macrosized pellet. Such a large-scale, bottom-up nanocrystal growth technique is more efficient than conventional nanofabrication and crystal growth techniques. The nanosheets have very high aspect ratios of nanometer thickness and millimeter lateral lengths (50,000: 50,000:1). Delaminated nanosheets are up to

$\sim$50 μm long. The length and shape of the nanosheets are uniform. The stacks of the $K_xCoO_2\cdot yH_2O$ nanosheets can be readily delaminated into free-standing nanosheets without altering crystal structure. The $K_xCoO_2\cdot yH_2O$ nanosheets show extreme ductility when mechanically bent. Electrical resistivity measurements of the $K_xCoO_2\cdot yH_2O$ nanosheet stacks indicate the resistivity is lower than $\sim$4.7 m$\Omega\cdot$cm at room temperature.

■ EXPERIMENTAL SECTION

Synthesis of $K_xCoO_2\cdot yH_2O$ Nanosheets. Appropriate quantities of poly(acrylic acid) (PAA, average molecular weight = $M_w \approx 1800$), cobalt(II) nitrate hexahydrate (0.230 M) and potassium carbonate (0.115 M) were dissolved in deionized water at room temperature. The K to Co ratio is set to 1. The ratio of PAA carboxylate groups to total metal ions is 1:2. The solution is evaporated at 150 °C on a hot plate with continuous stirring until it reached 20% of the initial volume. The resulting viscous, dark red solution is then autocombusted at 500 °C. The resulting black powder of homogenously mixed K and Co oxides is uniaxially pressed into pellets with a rectangular die set at 400 MPa. A typical size of the pellet is $10 \times 6 \times 5$ mm ($L \times W \times t$). The pellet is kinetically demixed for 72 h at $\sim$400 °C with a constant electrical current of 500 mA passing through Cu plates and contacts made of silver epoxy. Over the course of 72 h the voltage fluctuates between 20 and 5 V, and decreases by time. After the kinetic-demixing, the pellet separates into K-rich and K-depleted regions and the boundary between the two regions is clearly distinguishable. The K-depleted region is mechanically weak, porous and gray while the K-rich region is mechanically strong, dense, and black. The K-rich region of the pellet is separated and calcined in a tube furnace to obtain K_xCoO_2 nanosheets. The furnace is rapidly heated to 1000 °C and held for 30 min. The temperature is then ramped down to 970 °C in 1.5 h and after reaching 970 °C the furnace is allowed to cool down. The sample is removed from the furnace at around $\sim$700 °C and quickly evacuated in a vacuum desiccator to minimize $K_2CO_3\cdot1.5H_2O$ contamination. During the calcination the K-rich pellet is suspended on 0.25 diameter Au wires to limit the K and Co diffusion to the surrounding environment. K_xCoO_2 nanosheets form as stacks within the calcined pellet. The calcined pellet (nanosheet composite, consisting of large number of K_xCoO_2 nanosheet stacks) was immersed in liquid nitrogen to mechanically extract individual stacks of K_xCoO_2 nanosheets with $>$20 μm thickness (containing $>$1500 single nanosheets) and up to 2.1 mm length. The nanosheet stacks are then soaked in clean (18 MΩ), room temperature water (250 mL), and stirred using a magnetic stirrer for 4−5 days in order to obtain $K_xCoO_2\cdot yH_2O$ nanosheets. Unlike K_xCoO_2 nanosheets, water stabilized $K_xCoO_2\cdot yH_2O$ nanosheets are stable enough in atmospheric conditions to perform X-ray diffraction, electron microcopy and electrical resistivity measurements without formation of unwanted surface contamination during the measurement process.

Delamination of the Nanosheets. Delamination of the $K_xCoO_2\cdot yH_2O$ nanosheets is accomplished through ball milling. Stacks of $K_xCoO_2\cdot yH_2O$ nanosheets are ball milled in clean, room temperature water for 4−5 h with 5 mm diameter high-wear-resistant zirconia balls. The delaminated nanosheets are then filtered through a 600 mesh Cu TEM grid (carbon-free) and imaged on the same grid.

XRD, SEM, EDS, WDS, and TEM Characterization. All of the intermediate and final products of the synthesis procedure were examined by a high resolution ($\sim$1 nm at 2 keV) scanning electron microscope (SEM, LEO 1550 FESEM) and by X-ray diffraction (XRD). Conventional $2\theta-\theta$ XRD measurements were conducted using Rigaku Smartlab and Scintag (Pad-X) instruments and area detector XRD measurements was performed using Bruker General Area Detector Diffraction System. Cu Kα1 X-ray sources were used in all XRD characterization. To observe the texturing of the stacks of $K_xCoO_2\cdot yH_2O$ nanosheets, the nanosheet stacks were aligned perpendicular to X-ray scattering axis for the XRD measurements. For the XRD-based phase identification, the samples were ground before the XRD measurements in order to minimize possible texturing
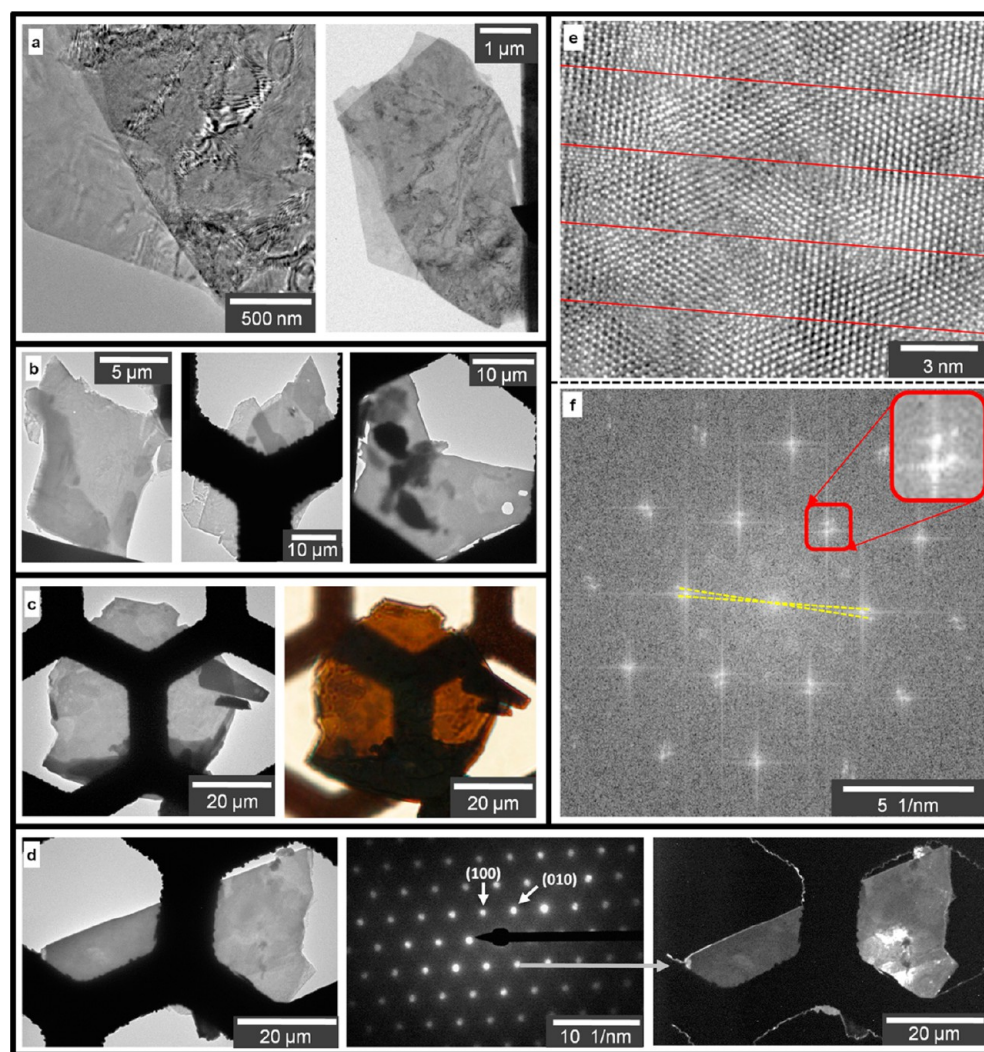
Figure 1. TEM, HR-TEM, and optical microscopy images of delaminated $K_xCoO_2 \cdot yH_2O$ nanosheets. (a) High (left) and low (right) magnification TEM images of delaminated nanosheets. (b) TEM images of thicker stacks of electron transparent delaminated nanosheets. (c) TEM image (left) of a large delaminated nanosheet ($\sim 45 \times 45$ μm) with optical microscopy image (right) of the same nanosheet under transmitted light. (d) TEM image (left) of a large, electron transparent nanosheet ($\sim 50 \times 20$ μm), ED pattern (middle) of the same nanosheet indicating that the nanosheet is crystalline and the orientation of cross-plane thickness is [001], dark-field image (right) confirming this ED pattern is representative of the entire sheet and that the nanosheet is a single crystalline. (e) HR-TEM image of a delaminated nanosheet (red parallel lines indicate Moiré fringes forming due to the rotational misalignment of the nanosheets around [001] axis). (f) FFT of the image in panel e showing the reciprocal lattice of the delaminated nanosheet. The inset image in panel f shows four nearby reciprocal lattice points originating from nanosheets with different a-axis lattice spacings (~ 2.6, ~ 2.8, and ~ 3.0 Å) and rotational alignments. Two yellow dashed lines are drawn between the reciprocal lattice points of two rotationally misaligned nanosheets. The angle between the dashed lines indicates 5.7° of rotational misalignment which closely matches with 5.5° of rotational misalignment obtained from the Moiré fringes in panel e. See Supporting Information, Figure S3, for more HR-TEM images of the delaminated nanosheets.

and crystal alignment effects which can alter relative intensities of different XRD peaks. For the XRD characterization of hygroscopic K_xCoO_2 nanosheets, the samples were first heated up to 500 °C to decompose the existing $K_2CO_3 \cdot 1.5H_2O$ contamination and then allowed to cool down to room temperature under ^{4}He gas flow. XRD measurements of K_xCoO_2 nanosheets were performed at room temperature under continuous ^{4}He gas flow to prevent formation of $K_2CO_3 \cdot 1.5H_2O$ contamination during the measurement. Transmission electron microscopy (TEM), dark field imaging, and electron diffraction were performed with an FEI T12 Spirit TEM at 120 kV accelerating voltage. High-resolution (HR) TEM images were taken with an FEI F20 TEM at 200 kV accelerating voltage. Elemental analyses were performed using an electron dispersive X-ray spectrometer (EDS) attached to a LEO 1550 FESEM and wavelength dispersive X-ray spectrometers (WDS) attached to a JEOL 8900 Microprobe. $KAlSi_3O_8$ and metallic Co are used as reference materials

in WDS characterization for high precision quantification of K/Co atomic ratio in $K_xCoO_2 \cdot yH_2O$ nanosheets.

Electrical Resistivity Measurements. Successful two-point resistivity measurements have been achieved by first cutting thin strips of double-sided Scotch Tape to widths comparable to the length of the nanosheet sample. This strip is adhered to a glass slide, and the nanosheet sample is placed on the strip of tape such that two opposing edges protrude past the tape on either side. Conductive silver paint is used to attach the nanosheet samples to four copper electrodes, two electrodes per edge (See Supporting Information, Figure S1). The electrodes are short lengths (~ 2 cm) of 0.08 mm diameter copper wire. The wires are first dipped in soldering flux to remove any native oxide on the copper metal. The silver paint is allowed to dry, and the sample is then connected for a 4-wire resistance measurement by using the four copper electrodes for the voltage and current contacts (see Figure 2 inset drawing). Once attached, the sample is placed in

vacuum at <10 microbar, submerged in a liquid nitrogen fridge, and slowly cooled to 160 K. A resistance measurement is taken every 5 K during cool down.

RESULTS AND DISCUSSION

The free-standing nanosheets were characterized by scanning electron microscope (SEM), energy dispersive X-ray spectroscopy (EDS), transmission electron microscope (TEM) and high resolution transmission electron microscope (HR-TEM). Very large $K_xCoO_2 \cdot yH_2O$ nanosheets are delaminated from pellets composed of millimeter-length stacked nanosheets (see methods). The free-standing nanosheets are typically 5−50 μm laterally, as determined by optical and transmission electron microscopy (Figure 1a, 1b, 1c, and 1d). Thin individual and stacked nanosheets are seen in Figure 1a. Typical nanosheet stacks with tens-of-micrometers lateral lengths are shown in Figure 1b. Under transmitted white light the delaminated nanosheets are translucent brown (Figure 1c (right)) as previously observed for Na_xCoO_2 nanosheets.[20] This delaminated nanosheet stack in Figure 1c is ∼170 nm thick based on SEM characterization (see Supporting Information, Figure S2), and contains ∼10 individual nanosheets. Selected area electron diffraction (SAED) from multiple regions of each 2D crystal confirm the hexagonal crystal symmetry with [001] being the zone axis. The well-defined, bright points in SAED (Figure 1d (middle)) indicate that the stacked nanosheet crystals are in registry with each other along the c-axis direction. TEM dark-field imaging from a hexagonal-lattice {100} diffraction spot shows that the entire sheet is single crystalline with the lateral length being along the ⟨100⟩ directions (Figure 1d (right)). The lattice spacing and hexagonal symmetry resulting from HR-TEM characterization of a nanosheet (Figure 1e) and its reciprocal lattice image derived through the Fast Fourier transform (FFT) (Figure 1f), indicates the nanosheets are crystalline for K_xCoO_2. Inspection of the reciprocal lattice points (Figure 1f, inset) indicate four different nanosheet crystals with three different a-axis lattice spacing values (∼2.6, ∼2.8, and ∼3.0 Å). These a-axis lattice spacing values are within ∼10% of the a-axis lattice spacing values previously reported for rhombohedral ($x = 0.5$) and hexagonal ($x = 0.61$ and 0.67) K_xCoO_2 phases.[30,31] The four distinct reciprocal lattice points in Figure 1f are located at three positions along the rotation axis around [001] indicating rotational misalignment of individual nanosheet crystals. The maximum angle of rotation between the reciprocal lattice points is ∼5.7° as visualized by the two yellow dashed lines in Figure 1f. Moiré fringes in the original crystal image (Figure 1e) also indicate a rotational misalignment ($\alpha = 2 \cdot \arcsin(p/2D) = 5.5°$, where p is d-spacing and D is the distance between Moiré fringes[38]) close to the maximum rotational misalignment observed in the FFT image. Similar Moiré patterns were also observed for rotationally misaligned multilayer graphene superlattices by several other groups.[38−40] The rotational misalignment of the nanosheets combined with their perfect registry along the c-axis indicate that the nanosheets are stacked on top of each other with "turbostratic arrangement". Such an arrangement was also previously observed for the stacking of Na_xCoO_2 nanosheets.[20]

Electrical resistivity measurements were performed on the as-grown stacks of water stabilized $K_xCoO_2 \cdot yH_2O$ nanosheets in a temperature range of 160 to 295 K. The two-point resistivity measurements were performed parallel to the nanosheets using two area contacts that are made on the sample with silver paint (see Figure 2 inset drawing). The size of the nanosheet stack

used in the measurement in Figure 2 is $730 \times 340 \times 6$ μm ($L \times W \times t$). The silver paint used for attaching the electrodes
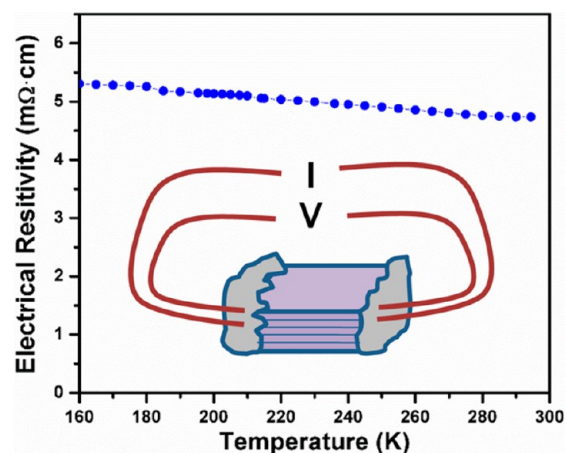

Figure 2. Temperature dependent electrical resistivity values for $K_xCoO_2 \cdot yH_2O$ nanosheets (blue dots). Inset figure shows the configuration for the electrical resistivity measurements. The measurements were performed parallel to the nanosheets using two area contacts. See Supporting Information, Figure S5 for optical microscopy and SEM images of the nanosheet stack used for the measurement.

encroaches into the sample by up to ∼290 μm in total from the two sides along the measurement axis resulting in an effective electrode separation of ∼440 μm. To obtain an upper limit for the in-plane resistivity value of the nanosheet stack, we assumed the electrode separation to be 440 μm. This calculation should provide an overestimation for the in-plane resistivity (ρ_{ab}) of the nanosheets for two more reasons: (1) The contact resistances at the interfaces between the silver paint and nanosheets are included in the two-point resistance measurement and (2) because the silver paint contacts are not perfectly affixed to only the surfaces of the {100} planes, the higher c-axis resistivity[34] will mix in with the lower in-plane values as has been seen previously in layered alkali cobaltates.[25] Figure 2 shows the measured in-plane electrical resistivity values for a stack of water stabilized $K_xCoO_2 \cdot yH_2O$ nanosheets. The single crystalline nature of the nanosheet stack along the measurement plane is critical for low electrical resistivity. As a comparison, polycrystalline samples measured with the same method result in resistivity values that are more than 2 orders of magnitude higher (see Supporting Information, Figure S4). At room temperature, the overestimated in-plane resistivity value of the $K_xCoO_2 \cdot yH_2O$ nanosheets (∼4.7 mΩ·cm) is approximately two times higher compared to the bulk value previously reported by Tang et al. for $K_{0.35}CoO_2 \cdot 0.34H_2O$ (∼2.3 mΩ·cm).[34] However, even with the overestimated in-plane resistivity values, the $K_xCoO_2 \cdot yH_2O$ nanosheets have a remarkably high electrical conductivity for metal oxide nanosheets. To our knowledge, among the metal oxide nanosheets reported so far, these millimeter-length $K_xCoO_2 \cdot yH_2O$ nanosheets have the highest electrical conductivity for metal oxide nanosheets longer than 10 μm. Overall, these nanosheets have the second highest electrical conductivity after RuO_2 nanosheets.[36,37]

The synthetic procedure for $K_xCoO_2 \cdot yH_2O$ nanosheets is similar to the SGKD synthetic procedure for Na_xCoO_2 nanosheets described in our previous work.[20] The nanosheet

9001

dx.doi.org/10.1021/am402064g | ACS Appl. Mater. Interfaces 2013, 5, 8998−9007

synthesis consists of (a) the Pechini-method coordination of metal ions, (b) pyrolysis into oxide flakes, (c) pressurized pellet formation, (d) electric-field (E-field) induced kinetic-demixing, and (e) calcination (Figure 3). K_xCoO_2 nanosheets are
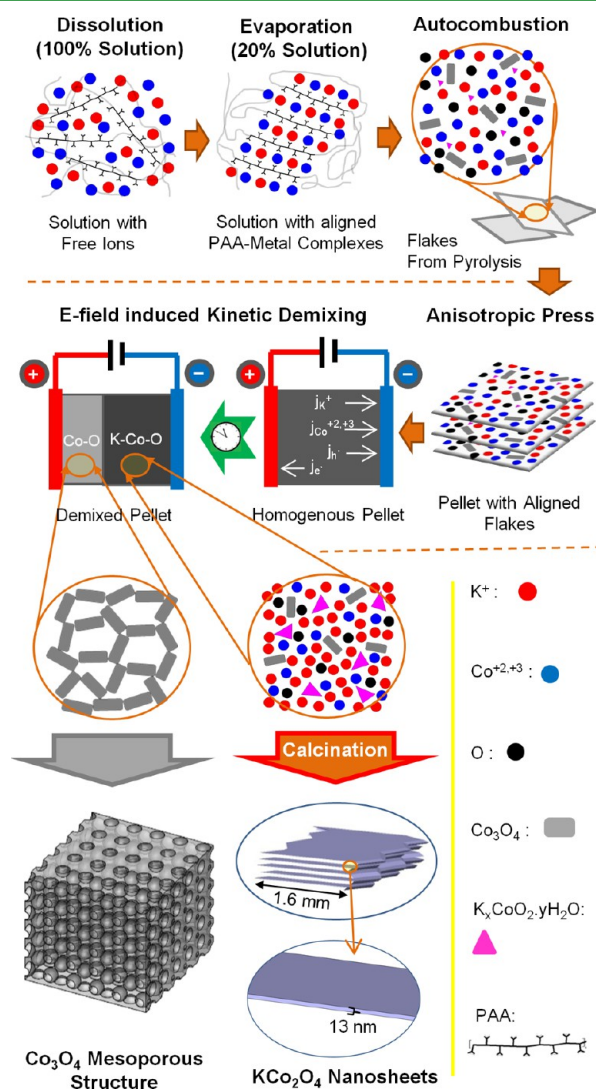

Figure 3. Schematic diagram of the nanomanufacturing procedure for millimeter-length $K_xCoO_2 \cdot yH_2O$ nanosheets. Metal precursors and poly(acrylic acid) are dissolved in water. The resulting solution is evaporated to ~80% of its initial volume, leading to an increase in viscosity and formation of metal complexes. The solution is autocombusted into a pyrolyzed phase, which form as flakes. The pyrolyzed flakes are uniaxially pressed into a rectangular pellet. Electric current is applied to the pellet, and kinetic-demixing occurs because of the difference in the mobilities of K and Co atoms. The K-deficient region is a porous network of Co_3O_4 particles. The K-rich region is calcined at 1000 °C leading to the formation of the nanolayered structure because of anisotropic grain growth.

obtained after calcination. The samples are then soaked in water for controlled hydration of the K_xCoO_2 nanosheets into the $K_xCoO_2 \cdot yH_2O$ phase. Finally, free-standing nanosheets of $K_xCoO_2 \cdot yH_2O$ are delaminated from the nanosheets stacks via ball milling.

In the first step of the synthesis the Pechini method[41] is modified to entrap the metal ions in solutions by using poly(acrylic acid) as the chelating agent. The metal cations are

expected to be stabilized by the chelating groups on the ligand, through dipole forces between water molecules and metal ions, and by the cross-linking and physical tangling of polymer chains which can trap both the cations and solvents in a drying polymer–metal ion complex sheet.[42−45] The structure of these polymeric entrapped layers is evident after the solution is pyrolyzed. SEM images show <200 nm thick and <400 μm long autocombusted flakes that include Co_3O_4 crystals with a relatively minor amount of $K_2CO_3 \cdot 1.5H_2O$ contamination according to the X-ray diffraction (XRD) pattern (Figure 4 and Supporting Information, Figure S6). Because of the highly hygroscopic nature of K−(Co)−O compounds, $K_2CO_3 \cdot 1.5H_2O$ contamination is observed in every step of the synthesis. To make measurements without the $K_2CO_3 \cdot 1.5H_2O$ contamination, the K atoms in the samples were stabilized within the
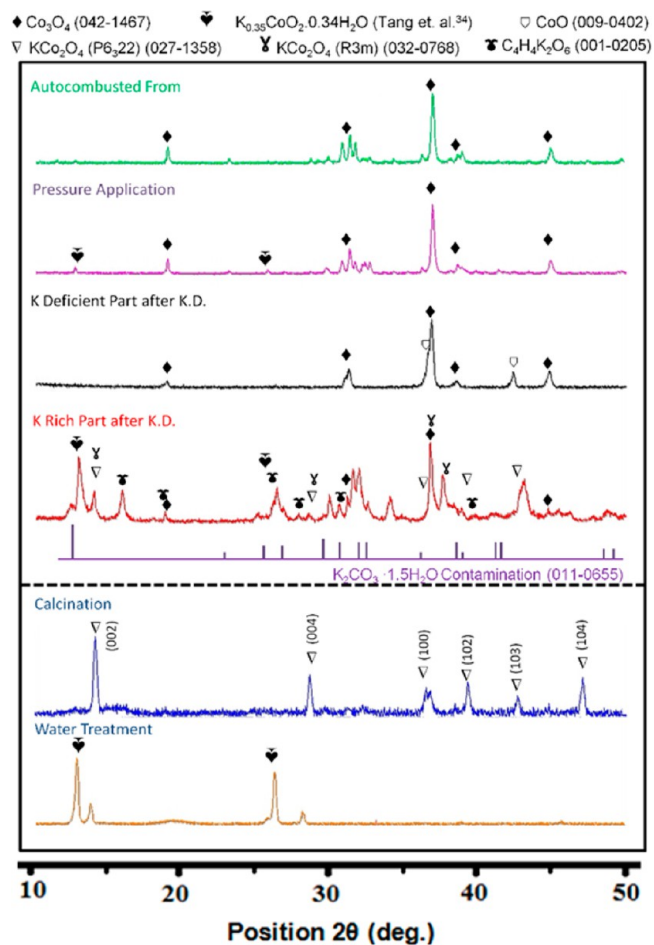

Figure 4. X-ray powder diffraction for each step of the nanosheet synthesis procedure (ordered from top to bottom). Pyrolyzed flakes after the autocombustion of the initial solution, anisotropically pressurized pellet of pyrolyzed flakes, K-deficient part of the pellet after E-field induced kinetic demixing, K-rich part of the pellet after E-field induced kinetic demixing, nanosheets after calcination of the K-rich part, water intercalated nanosheets after immersion of the calcined nanosheets in water. The samples in the form of pellets and nanosheet stacks were ground before the measurement. The peaks are identified for different phases with symbols and the available PDF numbers and/or references are listed for the phases in parentheses. Peaks without symbols are likely because of $K_2CO_3 \cdot 1.5H_2O$ contamination forming on the surface of K containing crystals. The reference peak positions for the $K_2CO_3 \cdot 1.5H_2O$ contamination are shown separately with purple lines.

sample through controlled water treatment or controlled atmosphere XRD measurement (Figure 4).

After the anisotropic pressure is applied to the autocombusted flakes by a rectangular die set, the XRD patterns indicate that the Co_3O_4 phase formed during the autocombustion is still present (Figure 4). However, after the pressurization process a distinct and relatively low intensity peak appears that closely matches with the peak positions reported by Tang et al. for the $K_{0.35}CoO_2 \cdot 0.34H_2O$ phase[34] (Figure 4). All of the peak intensities for both the autocombusted flakes and the pressurized pellet XRD are low, which can be due to the existence of amorphous materials in the sample in addition to the crystalline materials.

Performing E-field induced kinetic-demixing (Figure 5a) is the critical step to growing millimeter-length nanosheets. After application of a 500 mA current and a 1000 °C calcination, the nanosheet lateral lengths can reach ~2.1 mm. Samples with identical processing conditions but without kinetic-demixing do not contain nanosheets but arbitrarily shaped particles that reach only up to ~30 μm, that is, 70-times shorter (See Supporting Information, Figure S7). E-field induced kinetic-demixing occurs 4−5 times faster in the direction perpendicular to the pressure axis compared to the direction parallel to the pressure axis, most likely because the pressure-aligned flakes provide a more contiguous pathway for the current than the cross-plane pathway provides.

The E-field application to the homogeneous pellet results in an abrupt transition in K concentration along the E-field application axis and, according to XRD results, new phases form in the K-rich part of the pellet. Elemental analysis based on an SEM-EDS line scan shows the abrupt transition in K content and the morphology difference between the regions adjacent to the cathode and to the anode (Figure 5b and 5c). The region near the anode is K-depleted and extremely porous while the material near the cathode is K-rich and has a smooth unbroken surface (Figure 5b inset images, and Supporting Information, Figure S8). According to XRD, the K-deficient region is composed of only Co_3O_4 and CoO crystals while the K-rich region includes K−(Co)−O-based stoichiometric phases, such as KCo_2O_4 (both $R3m$ and $P6_322$), $K_{0.35}CoO_2 \cdot 0.34H_2O$, and $C_4H_4K_2O_6$, in addition to Co_3O_4 and $K_2CO_3 \cdot 1.5H_2O$ contamination (Figure 4).

The kinetic-demixing process produces a K saturated compound, which increases the Co diffusion coefficient during the high temperature (1000 °C) calcination, leading to the millimeter-length K_xCoO_2 nanosheets by anisotropic grain growth. Correlating the EDS data with the sample volume suggests that the K/Co ratio can be as high as 1.8 in the K-rich side. At high temperatures (~1000 °C), this K-rich part of the pellet shows molten fluidity that is evident from the pellet shape deformation (i.e., rectangular form into semispherical form) after the calcination (see Supporting Information, Figure S9). However, such shape deformation is not observed for the samples calcined directly after pressure application without the kinetic-demixing process (i.e., when the K/Co ratio is maintained at 1). The fluidity in the K saturated compound at high temperatures is associated with a significant increase in the Co diffusion coefficient. This increase in the Co diffusion coefficient can be explained by the temperature dependence of the Co diffusion coefficient and also the "physical correlation effect"[46] between the Co and K. Because of the "physical correlation effect", increasing the K content is expected to increase the diffusion coefficient of Co in the metal oxide
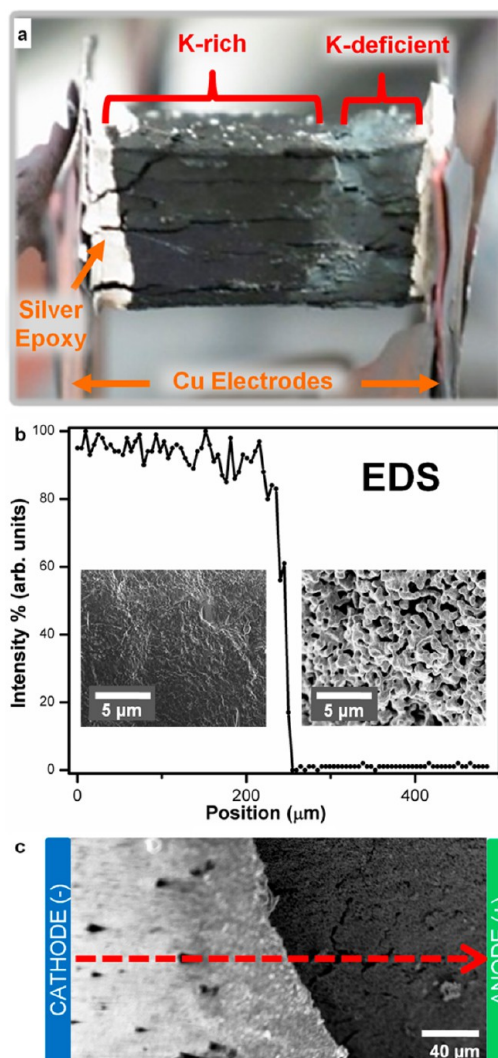

Figure 5. Characterization of the processing by electric-field induced kinetic-demixing. (a) Optical image of the anisotropically pressurized pellet of pyrolyzed flakes after E-field induced kinetic-demixing. An electric current passes through Cu plates and contacts made of silver epoxy. The potassium-rich (K-rich) and K-deficient parts of the pellet can be visually distinguished: the K-deficient region is gray in color and the K-rich region is black. (b) EDS line scan showing K concentration of the pellet after kinetic-demixing with respective SEM images of the K-deficient and K-rich regions. A stark contrast is seen between these regions: the K-deficient regions are more porous and contain nanograins while the surface of the K-rich region is smooth. (c) SEM image showing cracking between the two regions. The separation line corresponds to the abrupt jump shown in the EDS of panel b. Red dashed arrow shows direction of EDS scan.

mixture as previously proposed for a Na−(Co)−O mixture.[20,47] Our observation that high temperature molten fluidity exists only in kinetically demixed samples (i.e., if the samples were not kinetically demixed then there was no molten fluidity) points to increased diffusion from the physical correlation of a larger K/Co ratio. The Co diffusion amplification significantly reduces kinetic limitations, and leads to long nanosheet formation through cooperative effects including: facile grain growth, fluidity in the pellet during calcination, and enhancement of the anisotropic growth along the (001) plane.

$\theta-2\theta$ XRD patterns of K_xCoO_2 nanosheets obtained under inert atmosphere closely match with the KCo_2O_4 ($P6_322$)

9003

dx.doi.org/10.1021/am402064g | ACS Appl. Mater. Interfaces 2013, 5, 8998−9007
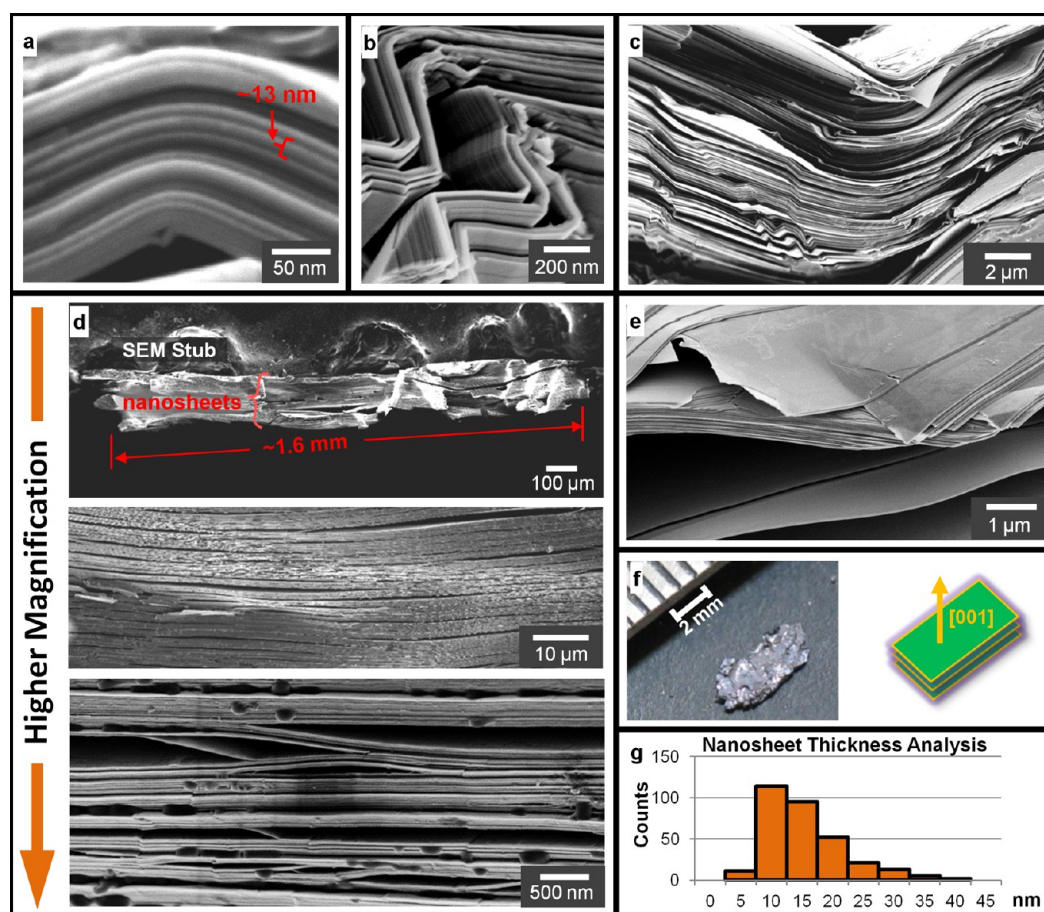
Figure 6. SEM and optical images of stacked nanosheets. (a) High magnification SEM image of the nanosheets showing the typical nanosheet thickness. (b) SEM image of metal oxide nanosheets displaying extreme ductility after mechanical bending. (c) Bending of relatively thick stack of metal oxide nanosheets (8−10 μm). (d) SEM images of nanosheet stacks from low magnification (top) to high magnification (bottom). Total nanosheet length is 1.6 mm, and stack thickness is nominally 100 μm. (e) SEM image of slightly bent $K_xCoO_2 \cdot yH_2O$ nanosheets showing smoothness of nanosheet surface. (f) (left) Optical image of a nanosheet stack obtained by mechanical extraction from the calcined bulk pellet. (right) The inset drawing shows the alignment of the nanosheets in the nanosheet stack. (g) Histogram of nanosheet thickness obtained by SEM based thickness measurements (314 nanosheets were measured in total resulting in ~13 nm thickness in average).

phase, according to the XRD studies that were performed after decomposing the surface $K_2CO_3 \cdot 1.5H_2O$ contamination. The XRD pattern of the calcined samples closely matches with the hexagonal KCo_2O_4 ($P6_322$) phase (Figure 4). The two adjacent peaks observed around ~36.6° indicate two different (100) lattice spacings (different by ~0.7%), while there is only one (002) lattice spacing according to the peak at 14.2°. Similar crystal structure was observed for Na_xCoO_2 nanosheets with grazing incidence X-ray diffraction measurements.[20]

SEM images of the metal oxide nanosheets are shown in Figure 6. A high magnification SEM image shows the typical $K_xCoO_2 \cdot yH_2O$ nanosheet thickness of ~13 nm with a standard deviation of 6.4 nm (Figure 6a and g, for the histogram of over 300 nanosheets that are measured by SEM). The nanosheet lateral lengths are several millimeters (Figure 6d and Supporting Information, Figure S10, show two different stacks of nanosheets with lengths ~1.6 mm and ~2.1 mm, respectively). The nanosheets demonstrate extreme ductility: Figure 6b shows nanoscale bending of the nanosheets (bending radius ~5 nm) and Figure 6c shows microscale bending of an 8−10 μm thick stack of nanosheets (bending radius ~5 μm). The nanosheets have a smooth surface (Figure 6e), implying a single crystalline nature. The nanosheet stacks (Figure 6d) consist of tens to hundreds of thousands of nanosheets, per

stack. An optical image of a mechanically extracted nanosheet stack is shown in Figure 6f.

After immersion of the calcined samples in DI water for 5 days, KCo_2O_4 nanosheets are converted to water stabilized $K_xCoO_2 \cdot yH_2O$ nanosheets. Water treatment of the nanosheets resulted in peak shifts in the XRD pattern toward smaller angles, which corresponds to an increase in the c-axis lattice spacing (Figure 4). This increase in atomic layer separation with water interaction is similar to what has been observed for the Na_xCoO_2 to $Na_xCoO_2 \cdot yH_2O$ transformation which occurs through the intercalation of water molecules between the two-dimensional triangular CoO_2 layers.[26,48] The two highest intensity peaks ($2\theta = 13.1°$ and $2\theta = 26.4°$) in the powder XRD pattern of the water stabilized nanosheets (Figure 4) closely match with the peak positions of (00L) planes reported by Tang et al. for the $K_{0.35}CoO_2 \cdot 0.34H_2O$ phase.[34] The other two peaks positioned at slightly higher angles ($2\theta = 14°$ and $2\theta = 28.3°$), compared to the first pair, are most likely associated with another set of (00L) planes of a secondary $K_xCoO_2 \cdot yH_2O$ phase with lower water content. The formation of the secondary phase was repeatedly observed for many samples from different synthesis batches without significant alteration of the XRD peak positions of the (00L) planes belonging to the $K_{0.35}CoO_2 \cdot 0.34H_2O$ phase and the secondary phase. Elemental

9004

dx.doi.org/10.1021/am402064g | ACS Appl. Mater. Interfaces 2013, 5, 8998−9007

analysis performed by WDS using reference samples (see Experimental Section) indicate that K/Co ratio for the water stabilized nanosheet stacks is ~0.44. This value is higher than the value found by Tang et al. through SEM-EDS.[34] The discrepancy may arise from the type or lack of reference samples used for the Tang et al. EDS characterization. The absence of all XRD peaks other than the (00L) planes (Figure 4, bottom) is likely due to highly anisotropic nature of the $K_xCoO_2 \cdot yH_2O$ crystals: with millimeter-length lateral sizes the nanosheet stacks show texturing through their alignment with the substrate and X-ray beam. Similar behavior was not observed in calcined samples because, unlike the water stabilized samples, the calcined samples were ground into arbitrary shaped submillimeter pieces without careful mechanical extraction of nanosheet stacks, resulting in a higher probability of random alignments for the crystals. Figure 7
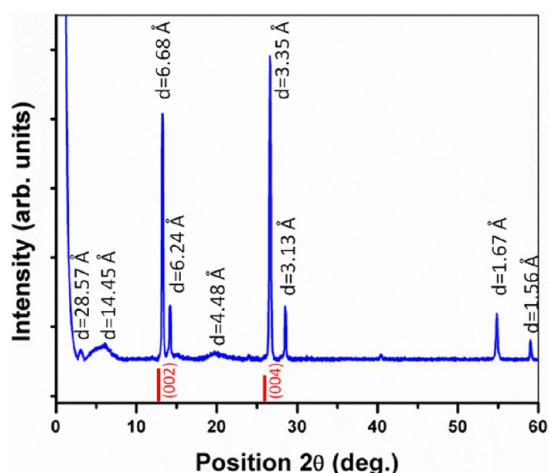

Figure 7. X-ray diffraction of a single stack of water intercalated nanosheets. The stacking axis of the nanosheets were aligned parallel to X-ray scattering vector ($Q \parallel c$-axis). d-spacing values are indicated for all peaks. The reference peak positions for the $K_{0.35}CoO_2 \cdot 0.34H_2O$ phase are shown with red stick lines.[34] Appearance of only (00L) peaks in the XRD pattern indicates that the nanosheets are large crystals and that they are strongly oriented (textured in alignment with respect to the incoming beam).

shows an X-ray diffraction pattern of a single stack of water stabilized nanosheets when the X-ray scattering vector (Q) is aligned perpendicular to the nanosheet stack. The peak positions in the XRD of the single stack of water stabilized nanosheets (Figure 7) match with the (00L) peak positions of the two different water intercalated phases observed in the powder XRD (Figure 4) of the same material. It is interesting that the two different phases are stable at the same time within a single stack of nanosheets. Considering the calculated d-spacing values, the peaks that appear at $2\theta = 54.8°$ and $2\theta = 59°$ in the XRD of the single stack of nanosheets are also associated with the same (00L) peaks observed in the powder XRD. On the other hand, the two wide, low intensity peaks at lower angles ($2\theta = 3.1°$ and $2\theta = 6.1°$) are likely associated with a separate set of (00L) peaks belonging to a third unknown phase. The peaks other than the (00L) peaks are absent because of texturing: the sample consists of a single nanosheet stack, and within the nanosheet stack the nanosheet crystals are well-aligned on top of each other.

X-ray diffraction studies performed using an area detector also indicate that nanosheet crystals are well-aligned along their

c-axes within the nanosheet stacks (Figure 8). In the area detector X-ray diffraction studies the angle between the sample stage and the incoming linear X-ray beam is tuned such that X-rays incline to the sample surface at $\theta = 6.55°$ (Figure 8a). The measurements are performed on a single nanosheet stack sample and, for comparison, on a polycrystalline sample. The single nanosheet stack sample is oriented on the sample stage such that the nanosheet stack top surface is parallel to the sample stage (i.e., the nanosheet stacking axis is perpendicular to the sample stage). The polycrystalline sample is prepared by uniaxially pressing many randomly oriented nanosheet stacks into a rectangular pellet (see Supporting Information Figure S4 caption). Area detector X-ray diffraction plots for the single nanosheet stack sample and the polycrystalline nanosheet sample are shown in Figure 8b and 8e, respectively, with the 2θ and χ axes marked. Distinct peaks along 2θ indicate diffraction from different lattice spacings and different peaks along χ indicate different crystal orientations. The spread of (00L) peaks along the χ axis in Figure 8b and 8e is an indication of different crystal orientations within the sample. The (00L) peak for the single nanosheet stack shows negligible spread along the χ axis (fwhm = ~3.6°) indicating that the nanosheet crystals are well-aligned on top of each other within the nanosheet stack and the nanosheet stack does not consist of randomly oriented nanosheets (Figure 8c). However, the large χ axis width (fwhm = ~78.4°) of the (00L) peak for the polycrystalline nanosheet sample indicates that that the polycrystalline nanosheet sample consists numerous nanosheets that are oriented along different directions (Figure 8f). The single nanosheet stack sample produces (00L) peaks only within close proximity of $2\theta = 13.1°$ because the incident X-ray beam inclines to nanosheet crystals at $\theta = 6.55°$ and the c-axes of all of the nanosheet crystals are well-aligned in the sample with negligible deviation. However, in the polycrystalline nanosheet sample (00L) peaks are observed at both $2\theta = 13.1°$ and $2\theta = 26.4°$ because the X-ray beam inclines to some of the randomly oriented crystals within the polycrystalline sample at 6.55° and some others at 13.2° satisfying the diffraction condition for both two 2θ peaks at 13.1° and 26.4°. Background noise is more apparent in the area detector X-ray diffraction plot of the polycrystalline nanosheet sample because the signal-to-noise ratio is significantly lower for the polycrystalline nanosheet sample compared to the single nanosheet stack sample, as expected for XRD signals of polycrystalline material compared to single crystal. XRD peaks from other crystal planes are not seen in the polycrystalline sample likely because of this poor signal-to-noise ratio. Optical images for both the single nanosheet stack sample and the polycrystalline nanosheet sample are shown in Figure 8d and 8g, respectively (only top surface can be seen in the image). The top surface of the single nanosheet stack has excessive dents and scratches mostly due to mechanical handling during the extraction of the nanosheet stack from the calcined pellet. The top surface of the polycrystalline sample shows multiple grains.

■ CONCLUSION

Electrically conductive, millimeter-length nanosheets of $K_xCoO_2 \cdot yH_2O$ were produced for the first time using the SGKD method. In-plane electrical resistivity of the $K_xCoO_2 \cdot yH_2O$ nanosheets is less than ~4.7 mΩ·cm at room temperature, which corresponds to the highest electrical conductivity in the literature for metal oxide nanosheets longer than 10 μm. The final product consists of tens of thousands of
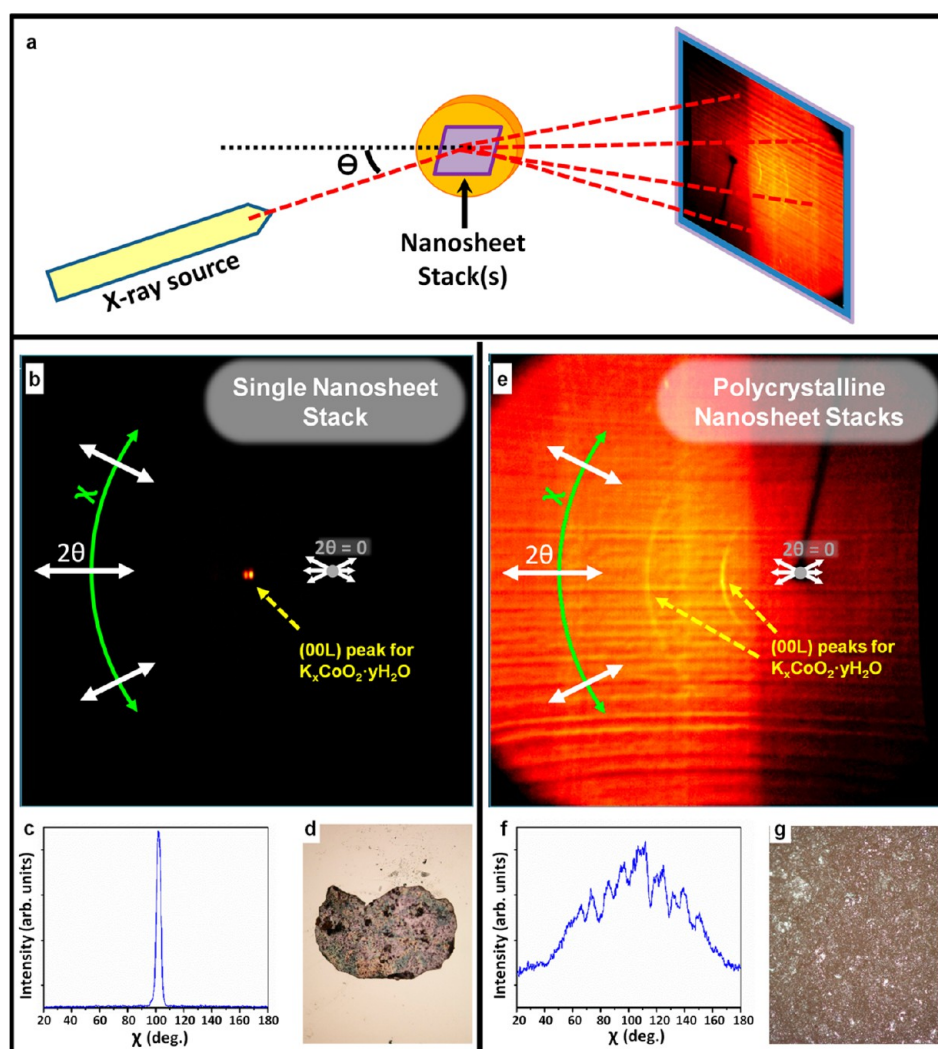
Figure 8. X-ray diffraction analysis of $K_xCoO_2 \cdot yH_2O$ nanosheet stacks using area detector: (a) Simplified schematics of the X-ray diffraction setup (see Supporting Information Methods 1). X-rays incline to the sample surface at $\theta = 6.55°$ and area detector is oriented to detect diffraction (2θ). The spot size of the X-ray beam is large enough to cover entire surface of the single nanosheet stack sample ($L \times W \approx 0.8 \times 0.5$ mm). The polycrystalline nanosheet sample is significantly larger than the post size of the X-ray beam. (b) Area detector X-ray diffraction plot from the single nanosheet stack mounted on Si wafer. (c) The intensity of the $2\theta = 13.1°$ (00L) peak from the $K_xCoO_2 \cdot yH_2O$ nanosheet stack is plotted against χ. The (00L) peak from the single nanosheet stack sample has negligible width (full width half maximum (fwhm) = ~3.6°) along the χ axis (instrumental broadening along χ is ~1.55°). (e) Area detector X-ray diffraction plot from the polycrystalline nanosheet sample. (f) The intensity for the $2\theta = 13.1°$ (00L) peak from the polycrystalline $K_xCoO_2 \cdot yH_2O$ nanosheet sample is plotted against χ. The fwhm of the (00L) $K_xCoO_2 \cdot yH_2O$ peak from the polycrystalline nanosheet sample is ~78.4°. (d and e) Optical images of the single nanosheet stack and the polycrystalline nanosheet samples used in the area detector X-ray diffraction experiment.

stacked nanosheets with extreme ductility, which makes a convenient form for device integration. The average thicknesses of the millimeter size nanosheets is ~13 nm resulting in a very high anisotropic aspect ratio (50,000: 50,000:1). The nanosheets can be easily mechanically bent, displaying their extreme ductility. The nanosheets are readily delaminated into freestanding sheets that are tens of micrometers long. Selected area electron diffraction studies indicated that the crystal properties are not altered by the delamination process. According to the HR-TEM characterization of delaminated nanosheets, the nanosheets are turbostratically stacked on top of each other. It should be able to synthesize nanosheets of other atomically layered oxides with this method.

ASSOCIATED CONTENT

Ⓢ Supporting Information

EDS analysis and additional SEM and HR-TEM images of the exfoliated nanosheets, additional SEM images of the nanosheet stacks, and SEM images regarding the intermediate products of the SGKD process and an optical image of the electrical resistivity measurement setup are available. This material is available free of charge via the Internet at http://pubs.acs.org.

AUTHOR INFORMATION

Corresponding Author

*E-mail: rdr82@cornell.edu.

Notes

The authors declare no competing financial interest.

■ REFERENCES

(1) Chen, X.; Zhang, N. Q.; Sun, K. N. *J. Phys. Chem. C* **2012**, *116*, 21224−21231.

(2) Nakato, T.; Nakamura, K.; Shimada, Y.; Shido, Y.; Houryu, T.; Iimura, Y.; Miyata, H. *J. Phys. Chem. C* **2011**, *115*, 8934−8939.

(3) Osada, M.; Sasaki, T. *J. Mater. Chem.* **2009**, *19*, 2503−2511.

(4) Coleman, J. N.; Lotya, M.; O'Neill, A.; Bergin, S. D.; King, P. J.; Khan, U.; Young, K.; Gaucher, A.; De, S.; Smith, R. J. *Science* **2011**, *331*, 568−571.

(5) Ma, R.; Sasaki, T. *Adv. Mater.* **2010**, *22*, 5082−5104.

(6) Takagaki, A.; Sugisawa, M.; Lu, D.; Kondo, J. N.; Hara, M.; Domen, K.; Hayashi, S. *J. Am. Chem. Soc.* **2003**, *125*, 5479−5485.

(7) Wang, L. Z.; Takada, K.; Kajiyama, A.; Onoda, M.; Michiue, Y.; Zhang, L. Q.; Watanabe, M.; Sasaki, T. *Chem. Mater.* **2003**, *15*, 4508−4514.

(8) Mas-Balleste, R.; Gomez-Navarro, C.; Gomez-Herrero, J.; Zamora, F. *Nanoscale* **2011**, *3*, 20−30.

(9) Butler, S. Z.; Hollen, S. M.; Cao, L.; Cui, Y.; Gupta, J. A.; Gutierrez, H. R.; Heinz, T. F.; Hong, S. S.; Huang, J.; Ismach, A. F.; et al. *ACS Nano* **2013**, *7*, 2898−2926.

(10) Tagusagawa, C.; Takagaki, A.; Hayashi, S.; Domen, K. *J. Phys. Chem. C* **2009**, *113*, 7831−7837.

(11) Zhang, Li; Tang, X.; Gao, W. *Cryst. Growth Des.* **2008**, *8*, 2489−2492.

(12) Sun, W. W.; Cao, F.; Liu, Y. M.; Zhao, X. Z.; Liu, X. G.; Yuan, J. K. *J. Mater. Chem.* **2012**, *22*, 20952−20957.

(13) Suzuki, S.; Miyayama, M. *J. Electrochem. Soc.* **2007**, *154*, A438−A443.

(14) Suzuki, S.; Miyayama, M. *J. Phys. Chem. B* **2006**, *110*, 4731−4734.

(15) Yeager, M.; Du, W. X.; Si, R.; Su, D.; Marinkovic, N.; Teng, X. W. *J. Phys. Chem. C* **2012**, *116*, 20173−20181.

(16) Osada, M.; Ebina, Y.; Funakubo, H.; Yokoyama, S.; Kiguchi, T.; Takada, K.; Sasaki, T. *Adv. Mater.* **2006**, *18*, 1023−1027.

(17) Osada, M.; Takanashi, G.; Li, B. W.; Akatsuka, K.; Ebina, Y.; Ono, K.; Funakubo, H.; Takada, K.; Sasaki, T. *Adv. Funct. Mater.* **2011**, *21*, 3482−3487.

(18) Osada, M.; Akatsuka, K.; Ebina, Y.; Funakubo, H.; Ono, K.; Takada, K.; Sasaki, T. *ACS Nano* **2010**, *4*, 5225−5232.

(19) Masuda, Y.; Hamada, Y.; Seo, W. S.; Koumoto, K. *J. Nanosci. Nanotechnol.* **2006**, *6*, 1632−1638.

(20) Aksit, M.; Toledo, D. P.; Robinson, R. D. *J. Mater. Chem.* **2012**, *22*, 5936−5944.

(21) Terasaki, I.; Sasago, Y.; Uchinokura, K. *Phys. Rev. B* **1997**, *56*, 12685−12687.

(22) Wang, Y. Y.; Rogado, N. S.; Cava, R. J.; Ong, N. P. *Nature* **2003**, *423*, 425−428.

(23) Shacklette, L. W.; Jow, T. R.; Townsend, L. *J. Electrochem. Soc.* **1988**, *135*, 2669−2674.

(24) Foo, M. L.; Wang, Y. Y.; Watauchi, S.; Zandbergen, H. W.; He, T.; Cava, R. J.; Ong, N. P. *Phys. Rev. Lett.* **2004**, *92*, 247001.

(25) Lee, M.; Viciu, L.; Li, L.; Wang, Y. Y.; Foo, M. L.; Watauchi, S.; Pascal, R. A.; Cava, R. J.; Ong, N. P. *Nat. Mater.* **2006**, *5*, 537−540.

(26) Takada, K.; Sakurai, H.; Takayama-Muromachi, E.; Izumi, F.; Dilanian, R. A.; Sasaki, T. *Nature* **2003**, *422*, 53−55.

(27) Liu, W.; Asheghi, M. *J. Appl. Phys.* **2005**, *98*, 123523−123526.

(28) Wang, Y. J.; Wilkinson, D. P.; Zhang, J. J. *Chem. Rev.* **2011**, *111*, 7625−7651.

(29) Pollet, M.; Blangero, M.; Doumerc, J. P.; Decourt, R.; Carlier, D.; Denage, C.; Delmas, C. *Inorg. Chem.* **2009**, *48*, 9671−9683.

(30) Delmas, C.; Fouassier, C.; Hagenmuller, P. *J. Solid State Chem.* **1975**, *13*, 165−171.

(31) Pollet, M. l.; Blangero, M.; Doumerc, J.-P.; Decourt, R.; Carlier, D.; Denage, C.; Delmas, C. *Inorg. Chem.* **2009**, *48*, 9671−9683.

(32) Nakamura, S.; Ohtake, J.; Yonezawa, N.; Iida, S. *J. Phys. Soc. Jpn.* **1996**, *65*, 358−360.

(33) Sugiyama, J.; Ikedo, Y.; Russo, P. L.; Nozaki, H.; Mukai, K.; Andreica, D.; Amato, A.; Blangero, M.; Delmas, C. *Phys. Rev. B* **2007**, *76*, No. 104412.

(34) Tang, H. Y.; Lin, H. Y.; Wang, M. J.; Liao, M. Y.; Liu, J. L.; Hsu, F. C.; Wu, M. K. *Chem. Mater.* **2005**, *17*, 2162−2164.

(35) Osada, M.; Sasaki, T. *Adv. Mater.* **2012**, *24*, 210−228.

(36) Sato, J.; Kato, H.; Kimura, M.; Fukuda, K.; Sugimoto, W. *Langmuir* **2010**, *26*, 18049−18054.

(37) Kim, D. S.; Ozawa, T. C.; Fukuda, K.; Ohshima, S.; Nakai, I.; Sasaki, T. *Chem. Mater.* **2011**, *23*, 2700−2702.

(38) Miller, D. L.; Kubista, K. D.; Rutter, G. M.; Ruan, M.; de Heer, W. A.; First, P. N.; Stroscio, J. A. *Phys. Rev. B* **2010**, *81*, No. 125427.

(39) Brown, L.; Hovden, R.; Huang, P.; Wojcik, M.; Muller, D. A.; Park, J. *Nano Lett.* **2012**, *12*, 1609−1615.

(40) Lu, C.-C.; Lin, Y.-C.; Liu, Z.; Yeh, C.-H.; Suenaga, K.; Chiu, P.-W. *ACS Nano* **2013**, *7*, 2587−2594.

(41) Pechini, M. P. Method of perparing lead and alkaline earth titanates and niobates and coating method using the same to form a capacitor. U.S. Patent 3,330,697, July 11, 1967.

(42) Kakihana, M. *J. Sol−Gel Sci. Technol.* **1996**, *6*, 7−55.

(43) Gulgun, M. A.; Nguyen, M. H.; Kriven, W. M. *J. Am. Ceram. Soc.* **1999**, *82*, 556−560.

(44) Gulgun, M. A.; Kriven, W. M.; Nguyen, M. H. Processes for preparing mixed metal oxide powders. U.S. Patent 6,482,387, Nov 19, 2002.

(45) Nguyen, M. H.; Lee, S. J.; Kriven, W. M. *J. Mater. Res.* **1999**, *14*, 3417−3426.

(46) Philibert, J. *Atom Movements: Diffusion and Mass Transport in Solids*; Les Éditions de Physique: Les Ulis, France, 1991; pp 77−83.

(47) Schnehage, M.; Dieckmann, R.; Schmalzried, H. *Bunsen-Ges. Phys. Chem., Ber.* **1982**, *86*, 1061−1065.

(48) Schaak, R. E.; Klimczuk, T.; Foo, M. L.; Cava, R. J. *Nature* **2003**, *424*, 527−529.